4-29-2019

Automatic Look-Up Table Based Real-Time Phase Unwrapping for Phase Measuring Profilometry and Optimal Reference Frequency Selection

Jianwen Song
Sichuan University, China

Daniel L. Lau
University of Kentucky, dllau@uky.edu

Yo-Sung Ho
Gwangju Institute of Science and Technology, South Korea

Kai Liu
Sichuan University, China

Published in *Optics Express*, v. 27, no. 9, 13357-13371.

Digital Object Identifier (DOI)
https://doi.org/10.1364/OE.27.013357

Research Article | Vol. 27, No. 9 | 29 Apr 2019 | OPTICS EXPRESS 13357
Optics EXPRESS

Automatic look-up table based real-time phase unwrapping for phase measuring profilometry and optimal reference frequency selection

JIANWEN SONG,[1] DANIEL L. LAU,[2] YO-SUNG HO,[3] AND KAI LIU[1,*]

[1]School of Electrical Engineering and Information, Sichuan University, Chengdu, 610065, China
[2]Department of Electrical Engineering, University of Kentucky, Lexington, KY, 40507, USA
[3]School of Electrical Engineering and Computer Science, Gwangju Institute of Science and Technology, Gwangju, 500-712, South Korea
[*]Corresponding author: kailiu@scu.edu.cn

Abstract: For temporal phase unwrapping in phase measuring profilometry, it has recently been reported that two phases with co-prime frequencies can be absolutely unwrapped using a look-up table; however, frequency selection and table construction has been performed manually without optimization. In this paper, a universal phase unwrapping method is proposed to unwrap phase flexibly and automatically by using geometric analysis, and thus we can programmatically build a one-dimensional or two-dimensional look-up table for arbitrary two co-prime frequencies to correctly unwrap phases in real time. Moreover, a phase error model related to the defocus effect is derived to figure out an optimal reference frequency co-prime to the principal frequency. Experimental results verify the correctness and computational efficiency of the proposed method.

1. Introduction

Phase measuring profilometry (PMP) is high speed and high accuracy three-dimensional (3-D) scanning technique where high, spatial-frequency, sinusoidal patterns are employed to suppress errors caused by sensor noise as well as projector/camera nonlinearities, but in order to avoid ambiguities in phase reconstruction, high-frequency phases must be correctly unwrapped. Compared with spatial phase unwrapping [1–4], temporal phase unwrapping [5–8] enjoys robust performance without suffering from phase discontinuities, phase jumps, and other distortions [9], but traditional temporal phase unwrapping methods [5, 7, 10, 11] typically need multi-frequency patterns, starting from unit-frequency. Although this procedure is very robust, the added patterns increase the total scan time as well as require more computation.

To shorten scan times and reduce computational complexity, two-frequency temporal phase unwrapping [12–16] has been developed. Long et al. [13] proposed a method for flexibly selecting wavelengths. Li et al. [14] proposed an optimal frequency selection algorithm for micro Fourier transform profilometry. Servin et al. [17] derived a phase-sum method to increase the signal-to-noise ratio (SNR). Li et al. [6] documented how frequencies could suppress noise and how to derive optimal frequencies. Hyun et al. [18] used geometric constraints to improve traditional two-frequency phase unwrapping. Now while all of above two-wavelength and two-frequency approaches have their benefits, they either sacrifice the SNR or need unit-frequency phase as a reference.

Using number theory, phase unwrapping with two co-prime frequencies was proposed by Gushov and Solodkin [19] who showed that only one reference phase map with a reference frequency co-prime to the principal frequency is needed to unambiguously unwrap a principal phase map. This approach was later simplified by Zhong et al. [20] and Ding et al. [21, 22] who established look-up tables (LUT) to simplify processing; however, the process of phase unwrapping needs a hand-made LUT storing the corresponding orders of wraps between the

#361004 https://doi.org/10.1364/OE.27.013357
Journal © 2019 Received 27 Feb 2019; revised 7 Apr 2019; accepted 8 Apr 2019; published 25 Apr 2019

Optics EXPRESS

reference patterns and the principal patterns. Once the principal frequency or/and the reference frequency is/are changed, the LUT has to be manually rebuilt.

In this paper first motivated by Ding et al. [21, 22] for two co-prime frequencies, we propose to unwrap phases in real time through a one-dimensional (1-D) LUT that is derived from a geometric model bridging the orders of wrapped phases. When frequencies are changed, this 1-D LUT will, therefore, be automatically updated. In order to further speed up phase unwrapping, this paper further proposes a two-dimensional (2-D) LUT that is derived based on the 1-D geometric model. Lastly, this paper proposes a means for setting the optimal reference frequency based on error analysis. Experimental results verify the correctness of the proposed method, our ability to perform reconstruction in real-time.

2. Phase measuring profilometry with phase unwrapping

Following the notation of Liu et al. [23] for PMP scanning, the projected sinusoid patterns are coded according to:

$$I_n^p\left(x^p, y^p\right) = A^p + B^p \cos\left[2\pi\left(f\frac{y^p}{H} - \frac{n}{N}\right)\right], \tag{1}$$

where I_n^p is the pattern intensity of a projector pixel at column and row coordinate (x^p, y^p), A^p and B^p are two constants such that $A^p \geq B^p$, f is the integer valued spatial frequency, H is the height of a projector's spatial resolution in rows, and n is the index of a phase shift with N (≥ 3) total phase shifts, respectively. After one pattern is projected onto a scanned object, a camera immediately captures an image and the patterned image, denoted as I_n^c, is modeled according to:

$$I_n^c\left(x^c, y^c\right) = A^c\left(x^c, y^c\right) + B^c\left(x^c, y^c\right)\cos\left[\phi\left(x^c, y^c\right) - \frac{2\pi n}{N}\right], \tag{2}$$

where A^c, B^c, and ϕ are direct component, intensity modulation, and phase, respectively, at camera coordinates (x^c, y^c). Note that I_n^c, A^c, B^c, and ϕ are functions of (x^c, y^c) which, henceforth, will be removed for simplifying notation.

The intensity of modulation, B^c, is a measure of the signal strength of the projected sinusoid, which is commonly used for removing shadow noise [23], and is computed according to:

$$B^c = \frac{2}{N}\sqrt{\left[\sum_{n=0}^{N-1} I_n^c \sin\left(\frac{2\pi n}{N}\right)\right]^2 + \left[\sum_{n=0}^{N-1} I_n^c \cos\left(\frac{2\pi n}{N}\right)\right]^2}. \tag{3}$$

The phase term, ϕ, is the phase of the projected sinusoid (measured spatially across the projector's vertical field of view), which is used for 3-D reconstruction, is computed according to:

$$\phi = \tan^{-1}\left[\frac{\sum_{n=0}^{N-1} I_n^c \sin\left(\frac{2\pi n}{N}\right)}{\sum_{n=0}^{N-1} I_n^c \cos\left(\frac{2\pi n}{N}\right)}\right], \tag{4}$$

which is mapped into $[0, 2\pi]$ according to our calibration strategy.

In practice, we set $f > 1$ in Eq. (1) to suppress various errors [24] but, consequentially, results in ϕ, computed by Eq. (4), to be exactly wrapped by the factor f and now needs to be unwrapped to cancel ambiguities. For wrapped ϕ shown in Fig. 1 (a), we follow the notation of Ding et al [21] and define the integer-valued $k \in [0, f-1]$, shown in Fig. 1(b), as the phase index such that the absolute phase, Φ, can be correctly unwrapped according to:

$$\Phi = \frac{\phi + 2k\pi}{f}, \tag{5}$$

Optics EXPRESS

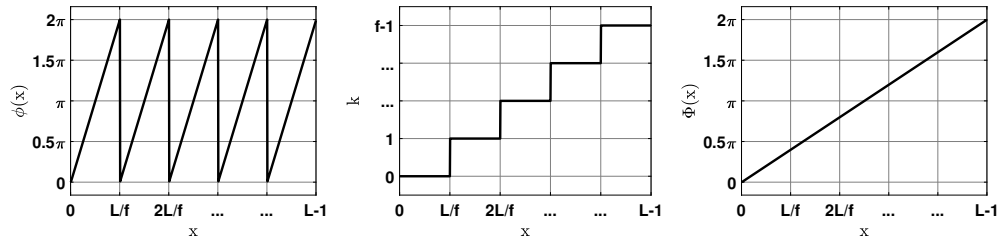

(a) (b) (c)

Fig. 1. The procedure of phase unwrapping: (a) Wrapped phase; (b) Order of wraps; (c) Unwrapped phase.

as shown in Fig. 1(c). In order to temporally unwrap ϕ, we can employ a reference phase denoted as ϕ^r and generated by another group of PMP patterns with a different frequency f^r. The reference frequency, f^r, needs to be a co-prime number to the wraps of ϕ [21, 22]. In Fig. 2(a), the dash-dot line is ϕ^r with wraps of $f^r = 3$. for example. Note that ϕ and ϕ^r can actually unwrap each other, and we call them as 'phase' and 'reference phase', respectively.

From Fig. 2(a) and for the originally computed ϕ and ϕ^r, it is difficult to visually figure out their relationship; however from the view of 1-D geometry, we know the equation for the curve of ϕ is defined according to:

$$\phi(x) = 2\pi \frac{f}{L}\left[(x) \bmod \left(\frac{L}{f}\right)\right] = 2\pi\left[\left(f\frac{x}{L}\right) \bmod (1)\right] = 2\pi\left(ft - \lfloor ft \rfloor\right), \tag{6}$$

where integer x is in the range $[0, L-1]$, integer t is equal to x/L, and mod$(\cdot)$ and $\lfloor\cdot\rfloor$ are the mathematical modulo and floor operations, respectively. Similarly, ϕ^r is defined according to:

$$\phi^r(x) = 2\pi\left(f^r t - \lfloor f^r t \rfloor\right). \tag{7}$$

With rescaling ϕ and ϕ^r by

$$\hat{\phi}(x) = \frac{f^r}{2\pi}\phi(x) = f^r\left(ft - \lfloor ft \rfloor\right) \tag{8}$$

and

$$\hat{\phi^r}(x) = \frac{f}{2\pi}\phi^r(x) = f\left(f^r t - \lfloor f^r t \rfloor\right), \tag{9}$$

respectively, we then have the difference between $\hat{\phi}$ and $\hat{\phi^r}$ defined according to:

$$\Delta(x) = \hat{\phi^r}(x) - \hat{\phi}(x) = f^r \lfloor ft \rfloor - f \lfloor f^r t \rfloor, \tag{10}$$

which are integers over $[-f^r+1, f-1]$ as shown in Fig. 2(b). For each interval $[kL/f, (k+1)L/f)$ with $k = 0, 1, \cdots, f-1$, the values of $\Delta(x)$ may look different, but they are equivalent and can be unified by

$$\hat{\Delta}(x) = [\Delta(x)] \bmod (f) = (f^r \lfloor ft \rfloor) \bmod (f) = (kf^r) \bmod (f), \tag{11}$$

for $k = 0, 1, \cdots, f-1$, as shown in Fig. 2(c).

For Eq. (11), although we can solve k from $\hat{\Delta}(x)$ by using analytical mathematical methods, e.g. Chinese remainder theorem [7], an alternative method, i.e. a LUT-based solution, is more efficient in practice. Two automatic LUT-based, i.e. 1-D and 2-D, strategies are proposed in this paper. Both are built with Eq. (11).

Optics EXPRESS

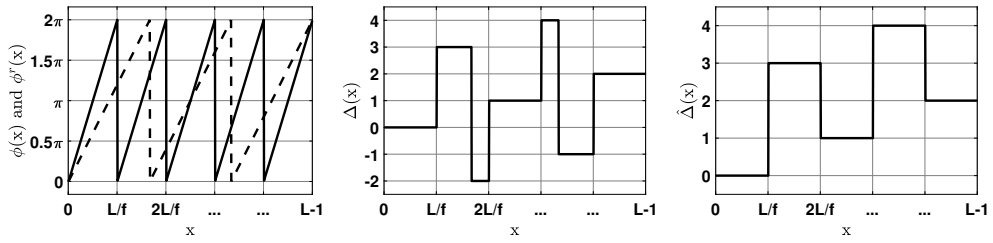

(a) (b) (c)

Fig. 2. The relationship between $\hat{\phi}$ and $\hat{\phi^r}$: (a) $\phi(x)$ and $\phi^r(x)$; (b) $\Delta(x)$; (c) $\hat{\Delta}(x)$.

2.1. One-dimensional look-up table

With known f and f^r, a 1-D LUT with length, f, can be automatically built directly from Eq. (11) according to:

$$\mathrm{LUT}\left[(k f^r) \bmod (f)\right] = k, \tag{12}$$

for $k = 0, 1, \cdots, f-1$. For example, if $f = 5$ and $f^r = 3$, the corresponding LUT is shown in Table 1. With $\hat{\Delta}(x)$ computed via Eq. (11) and the LUT previously built by using Eq. (12), we can access k by looking up the LUT immediately as

$$k = \mathrm{LUT}\left[\hat{\Delta}(x)\right], \tag{13}$$

and ϕ is finally unwrapped by using Eq. (5). Again, once f or f^r is changed, we can automatically update the LUT by using Eq. (12), and don't need to manually fill out a table.

Table 1. **A 1-D LUT with $f = 5$ and $f^r = 3$**

$(k f^r) \bmod (f)$	0	1	2	3	4
k	0	2	4	1	3

2.2. Two-dimensional look-up table

By observing Fig. 2(a), we note that each combination of fringe orders, for ϕ and ϕ^r, corresponds to phases in different ranges. For example, Fig. 3(a) shows wrapped phases for $f = 5$ and $f^r = 3$ from the view of 1-D geometry. The wrapped phases can be classified into 7 areas, and each area is a fixed combination of fringe orders. By setting ϕ^r versus ϕ as shown in Fig. 3(b), there are 7 parallel lines relating to wrapped phases of 7 areas in Fig. 3(a), i.e., the ranges of the combination of two wrapped phases in these 7 areas are different. Then, by deriving fringe orders from wrapped phases directly, we eliminate the need for calculating the phase difference as well as the modulo operation. Thus, we can establish a 2-D LUT to further speed up phase unwrapping.

As shown in Fig. 3(b), the intercept of each line, b_i, is defined according to:

$$b_i = \phi - \frac{f}{f^r}\phi^r, \tag{14}$$

where i is an integer-valued index for each line with range of $[1, f + f^r - 1]$. With Eqs. (8) and (9), we rescale ϕ and ϕ^r into $\hat{\phi} \in [0, f^r]$ and $\hat{\phi^r} \in [0, f]$, respectively. As the relationships among rescaled intercept $\hat{b}_i$ and fringe orders listed in Table 2, we have

$$\hat{b}_i = \hat{\phi} - \hat{\phi^r}, \tag{15}$$

Optics EXPRESS

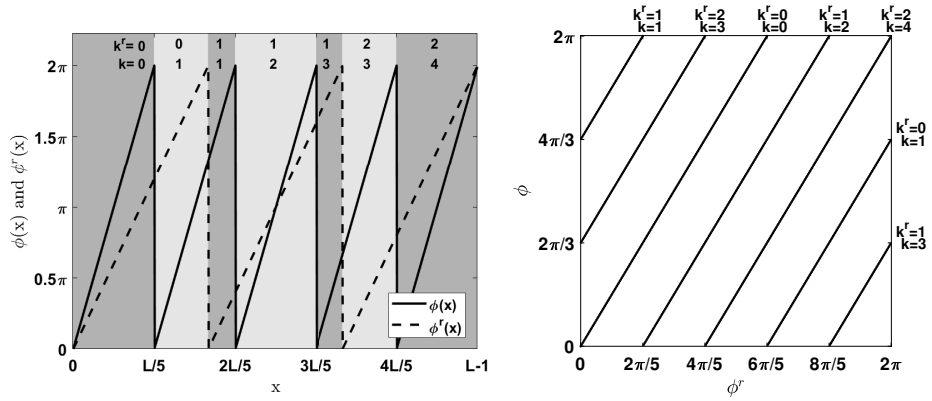

(a) (b)

Fig. 3. Two forms of wrapped phases: (a) Wrapped phases from the view of 1-D geometry; (b) Relationship between two wrapped phases using phase value as coordinate.

Table 2. **Rescaled Intercept and Its Corresponding Fringe Order**

$\hat{b}_i$	2	1	0	-1	-2	-3	-4
(k, k^r)	(1, 1)	(2, 3)	(0, 0)	(1, 2)	(2, 4)	(0, 1)	(1,3)

which is negative to $\Delta(x)$ in Eq. (10). For any unknown fringe orders of wrapped phases, we use Eq. (15) to compute rescaled intercepts and, similar to Eq. (11), unify the rescaled intercepts as indices to access fringe orders.

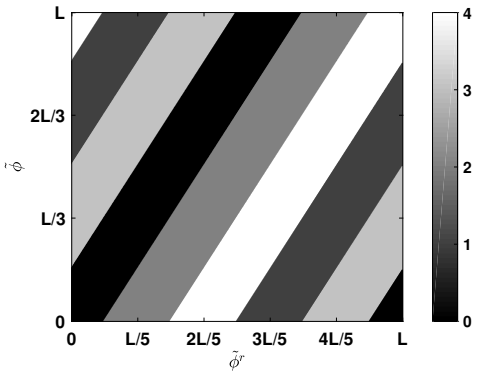

Fig. 4. A 2-D LUT with $f = 5$ and $f^r = 3$.

With Eq. (15) and the 1-D LUT built by using Eq. (12), we can enumerate all combinations of ϕ and ϕ^r over $[0, 2\pi]$. Since the indices of a LUT need to be integers, we normalize ϕ and ϕ^r by

$$\tilde{\phi} = \text{round}\left(\frac{L\phi}{2\pi}\right) \tag{16}$$

and

$$\tilde{\phi}^r = \text{round}\left(\frac{L\phi^r}{2\pi}\right), \tag{17}$$

Optics EXPRESS

where L is the length of captured patterns along the scanned direction. The ranges of $\tilde{\phi}$ and $\tilde{\phi}^r$ are in $[0, L-1]$. Thus for known f^r, f and L, a 2-D LUT with size $L \times L$ is automatically built according to:

$$\mathrm{LUT}[m,n] = \mathrm{1DLUT}\left\{\left[\mathrm{round}\left(\frac{mf - nf^r}{L}\right)\right] \bmod (f)\right\}, \tag{18}$$

where $m \in [0, L-1]$ and $n \in [0, L-1]$ are indices of the 2-D LUT and the 1-D LUT is established by using Eq. (12). Figure 4 shows an established 2-D LUT with $f = 5$ and $f^r = 3$.

2.3. Phase unwrapping algorithms

Our proposed phase unwrapping, using the 1-D and 2-D LUTs, is summarized by Algorithms 1 and 2, respectively.

Algorithm 1 Proposed phase unwrapping using a 1-D LUT

Input:
The principal frequency, f;
The reference frequency, f^r;
The captured patterns, I_n^c;
Output:
The absolute phase, Φ;
1: Build a 1-D LUT with f and f^r by using Eq. (11);
2: For ϕ and ϕ^r computed by using Eq. (4), rescale them to obtain $\hat{\phi}$ and $\hat{\phi}^r$ by using Eqs. (8) and (9);
3: Compute the difference between $\hat{\phi}$ and $\hat{\phi}^r$ by using Eq. (10) and then unify the difference by using Eq. (11) to obtain $\hat{\Delta}(x)$;
4: Use the values of $\hat{\Delta}(x)$ as indices to access orders, k, of wraps stored in the 1-D LUT built in Step 1;
5: With the orders k, finally obtain Φ by using Eq. (5);
6: If f or f^r is not changed, repeat Steps 2-5 for incoming I_n^c; otherwise Step 1 is needed.

Algorithm 2 Proposed phase unwrapping using a 2-D LUT

Input:
The principal frequency, f;
The reference frequency, f^r;
The length, L;
The captured patterns, I_n^c;
Output:
The absolute phase, Φ;
1: Build a 2-D LUT with f and f^r by using Eq. (18) and the 1-D LUT built with Eq. (11);
2: For ϕ and ϕ^r computed by using Eq. (4), rescale them obtain $\tilde{\phi}$ and $\tilde{\phi}^r$ by using Eqs. (16) and (17);
3: Use the values of $\tilde{\phi}$ and $\tilde{\phi}^r$ and as indices to access orders, k, of wraps stored in the 2-D LUT built in Step 1;
4: With the orders k, finally obtain Φ by using Eq. (5);
5: If f or f^r is not changed, repeat Steps 2-4 for incoming I_n^c; otherwise Step 1 is needed.

3. Optimal reference frequency selection

In this work, the principal frequency, i.e., the highest frequency, is typically fixed, while the reference frequency can be selected as any number co-prime to the principal. By analyzing errors causing errant phase unwrapping, this section derives a phase error model helping to determine an optimal reference frequency for the best phase unwrapping. Here, the term, $\hat{\Delta}(x)$, computed with Eq. (11) is correct only if, in Eq. (10), the error of $\Delta(x)$ is less than 0.5, or equivalently, the phase difference d satisfies:

$$d_{\phi^r} = \left| f\Delta_{\phi^r} - f^r\Delta_{\phi} \right| < \pi, \tag{19}$$

where Δ_{ϕ^r} and Δ_{ϕ} are the errors of ϕ^r and ϕ, respectively. These phase errors may derive from sensor noise [6, 25], gamma distortion [26], or projector/camera defocus [27]. Sensor noise is

Optics EXPRESS

not typically the main factor that influences phase unwrapping errors unless scanning at very low SNRs. Likewise, errors caused by gamma distortion are easy to avoid by increasing the number of shifts or taking an advanced calibration procedure [26].

Projector and/or camera defocus is, on the other hand, a dominant factor in relation to errors in phase unwrapping. The defocus procedure of an optical lens is typically modeled by a convolution operation resulting in blurred captured patterns [28], which is denoted as:

$$\hat{I}_n^c(x^c, y^c) = I_n^c(x^c, y^c) * g(x^c, y^c), \tag{20}$$

where the symbol $*$ represents convolution operation and $g(x, y)$ is a convolution kernel. Thus, the phase computed from blurred images is defined according to:

$$\hat{\phi}(x^c, y^c) = \tan^{-1}\left\{\frac{\sin[\phi(x^c, y^c)] * g(x^c, y^c)}{\cos[\phi(x^c, y^c)] * g(x^c, y^c)}\right\}, \tag{21}$$

where $g(x, y)$ is a point spread function (PSF) with Gaussian model. Here, we suppose the size of the PSF is 5×5 for facilitating our analysis.

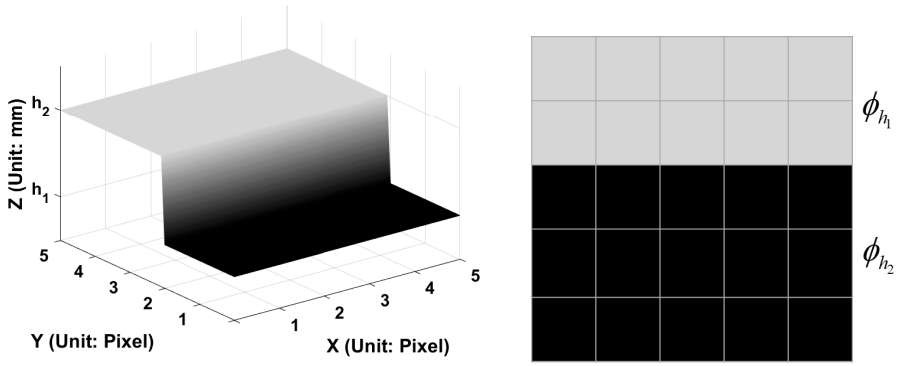

(a) (b)

Fig. 5. (a) Depth distribution of the 5×5 area; (b) Phase map of the 5×5 area.

Suppose one 5×5 area to be convolved by the PSF has the depth distribution shown in Fig. 5(a) with ten pixels in the first two rows having a depth of h_1 while the remaining fifteen pixels have a depth of h_2. The pixels with the same depth correspond to almost the same phase in a small area. As shown in Fig. 5(b), we treat the phases in the first two rows as ϕ_{h_1} and the remaining three rows as ϕ_{h_2}. Combining the elements in $g(x, y)$ with Eq. (21), the phase error at (x^c, y^c), i.e., the central location of the convolved area, is computed by

$$\begin{aligned}
\Delta_{\phi(x^c,y^c)} &= \phi(x^c, y^c) - \hat{\phi}(x^c, y^c) \\
&= \tan^{-1}\left\{\frac{\sum_{i=-1}^{1}\sum_{j=-1}^{1}\sin[\phi(x^c, y^c) - \phi(x^c - i, y^c - j)]\, g(i, j)}{\sum_{i=-1}^{1}\sum_{j=-1}^{j}\cos[\phi(x^c, y^c) - \phi(x^c - i, y^c - j)]\, g(i, j)}\right\} \\
&\approx \tan^{-1}\left\{\frac{g_1 \sin(\phi_d)}{g_1 \cos(\phi_d) + g_2}\right\},
\end{aligned} \tag{22}$$

where g_1 is the sum of first two rows in $g(x, y)$, g_2 is the sum of last three rows in $g(x, y)$, and ϕ_d is the difference between ϕ_{h_1} and ϕ_{h_2}. Because the sum of the elements in the $g(x, y)$ is 1 and $g(x, y)$ is symmetric, we know that $g_2 = 1 - g_1$ and g_1 is smaller than 0.5.

Optics EXPRESS

For one small area with slowly varied depths, the ϕ_d is small enough such that $\Delta_{\phi(x^c,y^c)}$ is nearly zero; however, in one small area with fast varying depths, the phase difference, ϕ_d, may be large, resulting in large d_{ϕ^r}. Actually, the value of ϕ_d depends on its specific position and the depths of the measured object. For phases computed from patterns of different frequencies, the value of ϕ_d is varied even for the same depth. The range of ϕ_d is $[-2\pi, 2\pi]$ since ϕ_d is computed from wrapped phases.

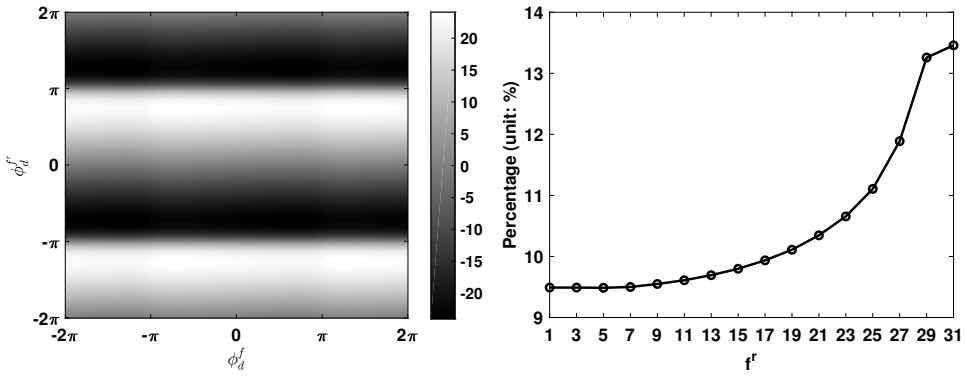

(a) (b)

Fig. 6. (a) Error map for $f^r = 1$; (b) Percentages of correct unwrapping points in the phase maps for different f^r.

Setting the principal frequency as $f = 32$, the reference frequency can be selected as one element of set $\{2r-1|r = 1, 2, \cdots, 16\}$. The ϕ_d of f and f^r, denoted as ϕ_d^f and $\phi_d^{f^r}$, respectively, can be any value in $[-2\pi, 2\pi]$. For all possible ϕ_d^f and $\phi_d^{f^r}$, the specific value of d_{ϕ^r} is easy to compute by using Eq. (19) with known g_1 and g_2. For example, with $g_1 = 0.4$, $g_2 = 0.6$ and $f^r = 1$, we can obtain an error map as shown in Fig. 6(a). Similarly, error maps of other reference frequencies can also be built.

Because the values of d_{ϕ^r} in the error map are certain, we can count the number of the points smaller than π, i.e., the number of correct phase unwrapping points in the error maps when the convolution effect exists. Then, the percentages of correct phase unwrapping points in the error maps for different f^r can be computed, as shown in Fig. 6(b), which can direct us to obtain a condition to achieve the largest phase unwrapping success rate. The larger the percentage, the less likely the phase unwrapping errors caused by the convolution effect will happen.

In the example shown in Fig. 6, the inferred optimal reference frequency is 31. Once the convolution parameters g_1 and g_2 are solved, we can infer an optimal reference frequency for the best phase unwrapping. The $g(x, y)$ can be expressed as a 2-D circular function according to:

$$g(x, y) = \frac{1}{2\pi\sigma} e^{-\frac{x^2+y^2}{2\sigma^2}}, \tag{23}$$

where σ is the standard deviation of the Gaussian distribution [29]. After obtaining the σ of the PSF, we can calculate the parameters g_1 and g_2 with the size of PSF. Actually, the size of PSF is merely to obtain the parameters g_1 and g_2 facilely. The circumstances of phase unwrapping errors are mainly surrounding discontinuous areas. For such areas, a PSF will influence the accuracy of phases only if the PSF is just falling on the central discontinuous areas, which means the PSF is nearly half and half distributing in the areas. So the values of g_1 and g_2 mainly depend on the standard deviation of the PSF.

The PSF is actually a low-pass filter such that the intensities of higher-frequency captured patterns have greater attenuation. The intensity modulation is a parameter which is significantly

Optics EXPRESS

affected by the PSF, and the attenuated intensity modulation can be expressed according to:

$$\hat{B}_f^c = B_0^c e^{-2\pi^2\sigma^2 f^2}, \tag{24}$$

where B_0^c is the uninfluenced intensity modulation [29]. Motivated by the method in [29], we use a combination of attenuated intensity modulation, $\hat{B}_f^c$ and $\hat{B}_{f^r}^c$, generated by patterns of f and f^r, respectively, to evaluate the σ with

$$\sigma = \sqrt{\frac{\ln\left(\hat{B}_{f^r}^c / \hat{B}_f^c\right)}{2\pi^2\left[f^2 - (f^r)^2\right]}}. \tag{25}$$

Combining the known σ with Eq. (23), the values of $g(x, y)$ can be obtained for the size of 5×5. After building the error maps with known g_1 and g_2, we can count the percentages of correct unwrapping points in the phase maps for different f^r similar to Fig. 6(b). Then, the optimal reference frequency is easy to infer.

4. Experimental results

In this section, experiments are conducted to verify the effectiveness of proposed phase unwrapping and the correctness of error analysis in Sec. 3. The PMP scanner consists of a Casio XJ-M140 projector, an AVT Prosilica GC650 camera, and a computer as the controller. The resolution of projector and camera are set as 800×600 and 640×480, respectively, and the camera works in grayscale mode. The software is programmed by using C++ language.

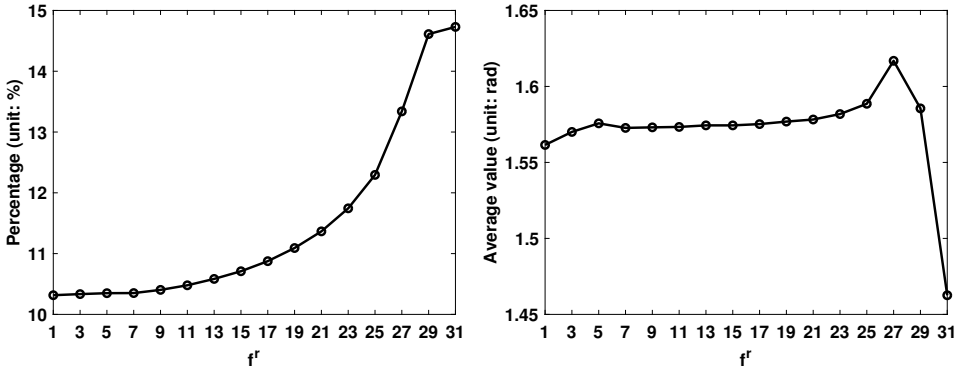

(a) (b)

Fig. 7. (a) Percentages of correct unwrapping points in the phase maps for different f^r; (b) Average values of error less than π for different f^r.

First and in order to determine an optimal reference frequency, we conduct a group of experiments using patterns with the following settings: $N = 16$, $A^p = B^p = 127.5$, principal frequency $f = 8$, and reference frequency $f^r = 1$. The scanned object is a white wall. Before scanning, the projector is well focused on the wall. After capturing the patterned images from the view of camera, we compute the attenuated intensity modulations, $\hat{B}_{f^r}^c$ and $\hat{B}_f^c$, with the size of 640×480 by using Eq. (3). Then, we take the average of the central 560×400 pixels in the original $\hat{B}_{f^r}^c$ and $\hat{B}_f^c$ as the final $\hat{B}_{f^r}^c$ and $\hat{B}_f^c$ to evaluate σ by using Eq. (25). In the experiments, the estimated σ is 2.31. With $\sigma = 2.31$ and the size of 5×5, the values of $g(x, y)$ are obtained by using Eq. (23) and the parameters g_1 and g_2 are 0.38 and 0.62, respectively.

The σ may slightly vary for different distances to the camera; however, the percentages of correct unwrapping points have almost the same trends for g_1 around 0.38. The final principal

Optics EXPRESS

frequency we choose is 32 and the percentages of correct points in the phase error maps for different f^r are shown in Fig. 7(a). The percentage increases slowly over the first several frequencies, then increases fast as the frequency becomes larger, reaching its highest point at $f^r = 31$. The percentages represent the probabilities of successful phase unwrapping when the convolution effect exists, which means the circumstance of $f^r = 31$ is less likely to meet phase unwrapping errors than the others. Moreover, we compute the average values of the points in error maps less than π for different f^r, and these results are shown in Fig. 7(b). The average value is of the lowest for $f^r = 31$. Such results show us the denoising ability of those correct unwrapping points in error maps partly. The smaller the average value, the better the denoising ability. Thus, we infer the optimal reference frequency for $f = 32$ is $f^r = 31$.

To verify the correctness of the proposed phase unwrapping and the optimal reference frequency we infer, we conduct other groups of experiments. First, we use the proposed method with the 2-D LUT for phase unwrapping. The basic settings of the projected patterns are as follows: $N = 16$, $A^p = B^p = 127.5$, a principal frequency $f = 32$, and a reference frequency that is one element from the set $\{2r - 1 | r = 1, 2, \cdots, 16\}$. The phases affected by gamma distortion and noise are ignorable under such setting. The scanned object is also a white wall. We employ the fringe orders computed by multi-frequency phase unwrapping method [5] with patterns of all frequencies as the ground truth.

Following the proposed phase unwrapping using the 2-D LUT step-by-step, we can obtain the measured fringe orders. We choose L as 480, i.e., the height of the captured patterns, which is also the largest resolution of the phase along the scanning direction. Thus, the success rates of phase unwrapping for different f^r can be counted. Consequently, the success rates are all 100% for each f^r, because the scanned object is a flat white wall with no discontinuous areas, performing successful phase unwrapping. The circumstance of $f^r = 1$ in the experiment is the same as multi-frequency method using two-frequencies, i.e., traditional two-frequency method.

According to the above results, our method achieves the same success rate as multi-frequency method when the scanned object is plane. Though the way of establishing the LUT in [21] is different from ours, their fringe orders are also accessed by using Eq. (10). So, our method

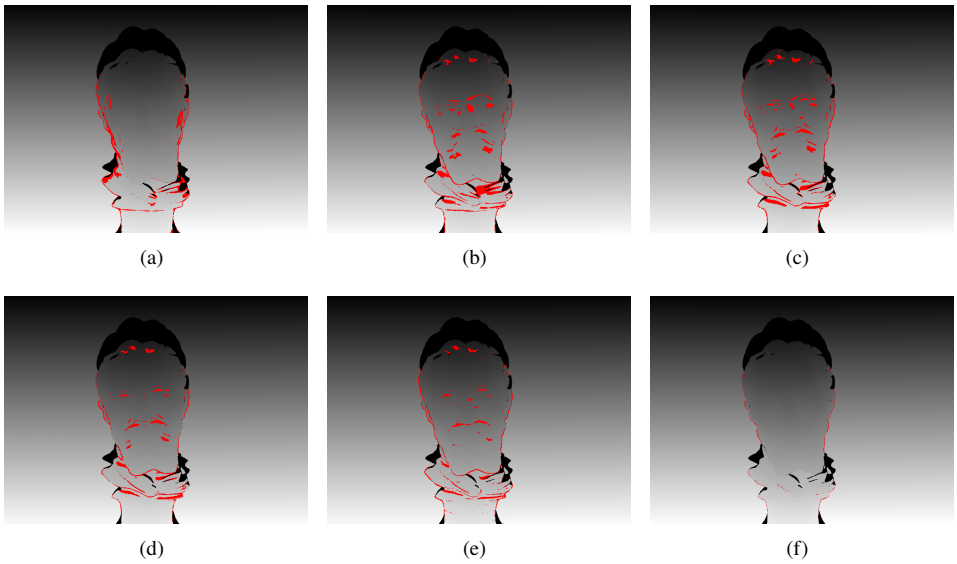

Fig. 8. Unwrapped phases with error markers for: (a) $f^r = 1$; (b) $f^r = 7$; (c) $f^r = 13$; (d) $f^r = 19$; (e) $f^r = 25$; (f) $f^r = 31$.

Optics EXPRESS

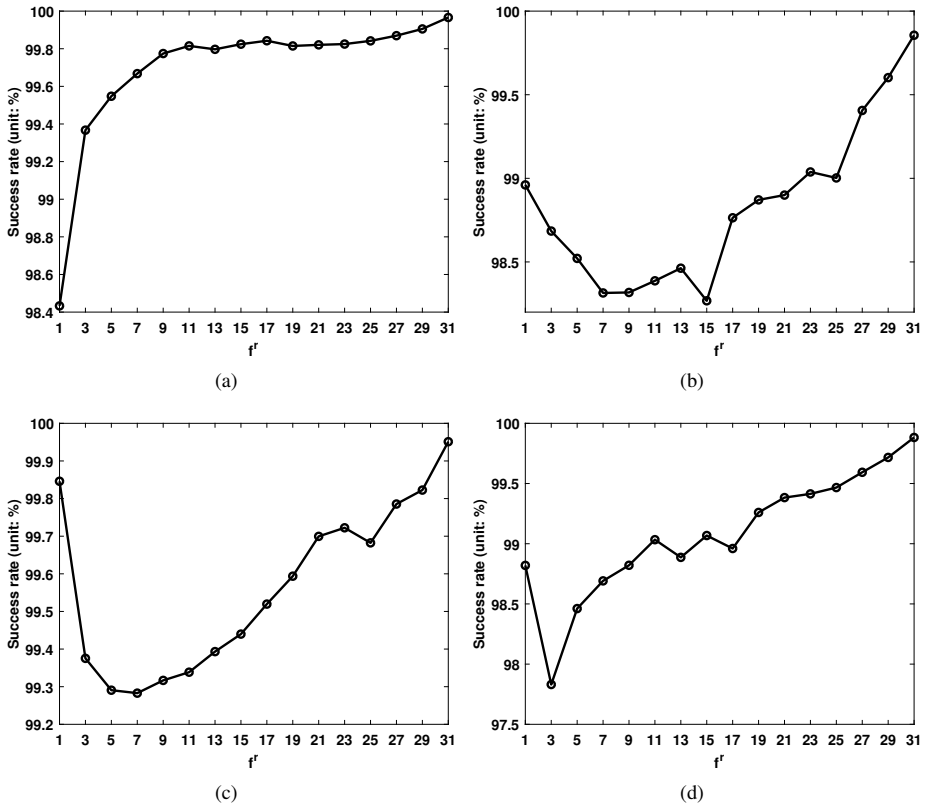

Fig. 9. Success rate of: (a) Plastic horse; (b) Michelangelo plaster statue; (c) Calibration target; (d) Cotton duck.

achieves the same success rate as the method in [21]; however, the steps of the method in [21] needs an ergodic process to search the corresponding fringe orders, which is much more time-consuming than our proposed LUTs.

For more interesting experiments, we changed the scanned target to either of four objects: a plastic horse; a Michelangelo plaster statue; a calibration target; and a cotton duck. The basic setting for projected patterns is the same as the just performed experiment. Similar to the above, the measured fringe orders and the ground truth are computed, respectively. The unwrapped phases of the Michelangelo plaster statue for different f^r are displayed in Fig. 8 with the red markers representing wrongly unwrapped points. The shadow noises in the principal phase and each reference phase are removed by using B^c, computed by Eq. (3), with a threshold of 10. As we can see, most incorrectly unwrapped points are surrounding an edge, the nose, and the eye areas, consistent with the analysis in Sec. 3 where the defocus of camera is a dominant effect when the depth variations are fast. The error points for $f^r = 31$ are few and much less than that of the others. Moreover, the success rates are shown in Fig. 9 where success rates of the Michelangelo plaster statue, the calibration target, and the cotton duck have the trend of decreasing first, then increasing as f^r increases.

In contrast, the success rate of the plastic horse has the trend of increasing as f^r increases. By observing the denoising ability shown in Fig. 7(b) when convolution effect exists, the average value of error less than π for $f^r = 1$ is not the largest and has the trend of increasing for $f^r < 27$. The average value achieves smallest for $f^r = 31$ and the value is much smaller than that of other f^r. Combining the ability to denoise with the percentages of successful phase unwrapping points

Optics EXPRESS

in the error maps when convolution exists, the final success rate may not be smallest for $f^r = 1$, while the success rate of $f^r = 31$ is the largest since both the two curves in Fig. 7 indicate us that the optimal reference frequency is $f^r = 31$. Eventually, all four of these groups of experiments achieve the highest success rate when $f^r = 31$. Such results are consistent with our inference about setting the optimal reference frequency.

Table 3 lists the specific success rates for $f^r = 1$ and $f^r = 31$ in different groups of experiments. The success rate for $f^r = 31$ are close to 100% and both of them are much better than that for $f^r = 1$. Therefore, the proposed method offers not only a flexible frequency combination but also a better phase unwrapping success rate than the traditional two-frequency method. Finally for the four objects, we use the Φ unwrapped via ϕ^r with $f^r = 31$ to reconstruct the 3-D point clouds with the front and side views shown in Fig. 10. There are just a few dissociative points caused by phase unwrapping errors surrounding the edges of each object. The main parts of each object are reconstructed well.

Table 3. **Success Rate for $f^r = 1$ and $f^r = 31$**

Object	Horse	Statue	Target	Duck
Success rate for $f^r = 1$(unit: %)	98.43	98.96	99.85	98.82
Success rate for $f^r = 31$ (unit: %)	99.96	99.86	99.95	99.88

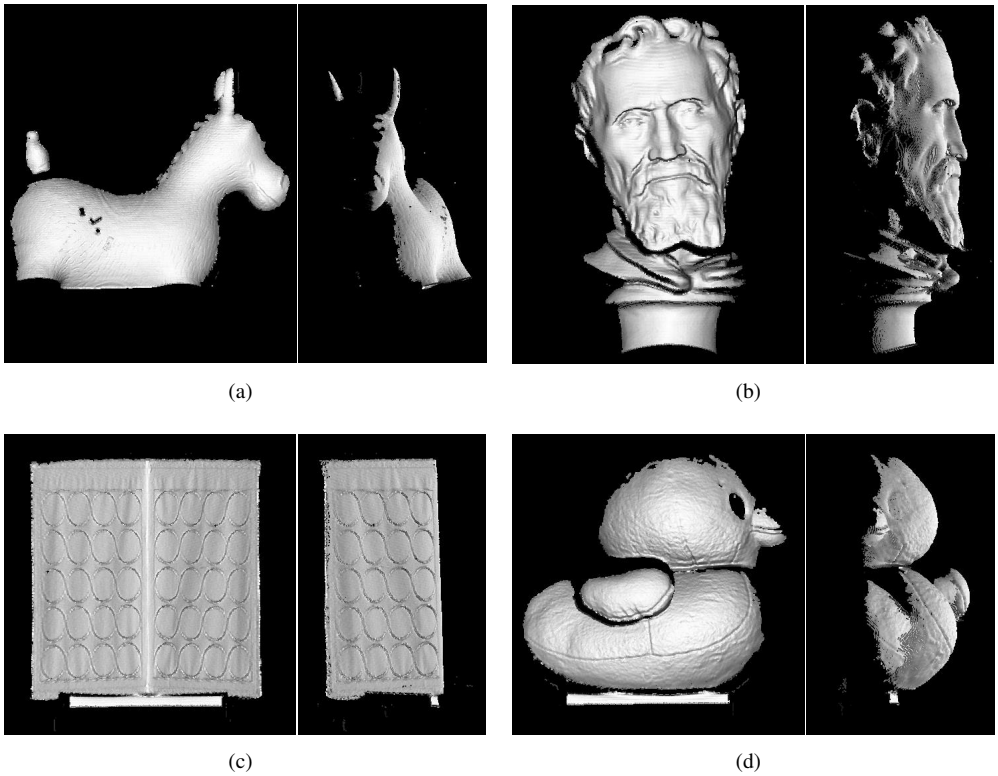

(a) (b) (c) (d)

Fig. 10. Reconstructed 3-D point clouds with $f^r = 31$: (a) Plastic horse; (b) Michelangelo plaster statue; (c) Calibration target; (d) Cotton duck.

As a last illustration, we conducted a group of experiments to compare the efficiency of the

Optics EXPRESS

traditional multi-frequency method [5], Ding's method in [21], and the proposed method using the 1-D LUT and the 2-D LUT, respectively. The calculation process is programmed by C++ language and running on a computer with 3.2 GHz Intel i5-6500 CPU, 16 GB RAM. The basic settings of the projected patterns are the same as the above experiments. The wrapped phases come from experiments on the Michelangelo plaster statue. According to the results of the above experiments, the accuracy of phase unwrapping for multi-frequency with two frequencies is fixed and the proposed method can get better performance on phase unwrapping because of flexible reference frequency usage. If the multi-frequency method achieves the same accuracy of phase unwrapping as the proposed method, more patterns are needed, which will sacrifice the time of scanning and calculating phases. Table 4 lists the number of needed patterns if all the methods achieve the success rate larger than 99.80%. Under such a success rate, we do 1000× experiments for each method with the average time cost of phase unwrapping compared, as shown in Table 4. If we take the time on scanning and calculating wrapped phases into consideration, the multi-frequency method will take much longer to complete since many more patterns are needed.

Table 4. **The Number of Need Patterns When the Success Rate is Larger Than 99.80% and Time Cost of Phase Unwrapping using Different Phase Unwrapping Methods**

Method	Multi-frequency [5]	Ding [21]	1-D LUT	2-D LUT
The number of needed patterns	64	32	32	32
Time cost	2.578ms	10.328ms	1.641ms	1.047ms

Table 4 shows us that the time of performing the 1-D LUT algorithm and 2-D LUT algorithm is much shorter than that of the multi-frequency method or Ding's method [21], and the time cost of 2-D LUT algorithm has improved 36.20% over the 1-D. The 1-D LUT algorithm needs to compute the extra phase difference, while the computed two wrapped phases can just be the indices of the 2-D LUT. Replacing time cost by space cost is more efficient in practical usage. As the above analysis shows, Ding's method needs an ergodic process to find the corresponding fringe orders, which is very time-consuming. The experimental results verify such analysis and with the proposed phase unwrapping using the 2-D LUT only spending 10.14% the time of Ding's LUT. So, the proposed phase unwrapping procedure using the 2-D LUT can be more effective in application and can meet the criteria of real-time PMP.

Now while the size of the 2-D LUT is much larger than that of 1-D LUT, our experiments verify that the speed of accessing fringe order in the 2-D LUT is much faster. The strategy of replacing time complexity by space complexity is effective, and the size, $L \times L$, is not very space-consuming. The usage of proposed LUTs is just an accessing process where the size of the LUT hardly influences the speed of phase unwrapping. Also by comparing the success rates for different L, we find that L does not have a significant impact on the phase unwrapping results. The biggest difference between two success rates for different L is small and will not be reflected in the percentage of two decimals, which is ignored in this paper. Though different L may raise quantization error because of the rounding operation, only the indexed points really close to the boundary of its stripe in the 2-D LUT may incur phase unwrapping errors caused by the quantization error and such circumstance seldom happens. So, we just choose L as the height of the captured patterns, which is also the largest resolution of the phase along the scanning direction.

Additionally, though we suppress the gamma distortion by increasing N in our work, the gamma distortion could influence the proposed phase unwrapping method if it is large. After conducting groups of experiments on a plane wall with $f = 32$ and $N = 3$, we find that the success rates

Optics EXPRESS

for different f^r are all smaller than 30%, which means destructive errors of phase unwrapping. Moreover, when changing N to 4, all the success rates become almost 100%. Then, we select the highest frequency as 23, 13, 7, and 5, respectively. The success rates are increasing as the highest frequency decreases. Only when the highest frequency is 5, the success rates of $f^r = 1, 3, 4$ achieve 100% and the results of other highest frequencies are not ideal. It has been proved that the amplitude of wrapped phase error caused by gamma distortion has no relation with frequency and the phase error is periodically varied along the scanning direction [26]. Substituting the wrapped phase error caused by gamma distortion into Eq. (19), the phase difference d_{ϕ^r} fluctuates rapidly in the range of $[-(f + f^r)|\Delta_\phi|_{\max}, (f + f^r)|\Delta_\phi|_{\max}]$. Thus, if gamma distortion is large enough, there will be destructive errors of phase unwrapping, i.e., a large number of points in the wrapped phase will be wrongly unwrapped. Also, if the highest frequency is set as a small number which can avoid phase unwrapping error caused by gamma distortion, the unwrapped phase will still suffer from errors, resulting in unreliable 3-D reconstruction. Actually, such phenomena are not just happening in the proposed phase unwrapping method. For other temporal phase unwrapping methods, if the highest frequency is much larger than the low frequency, the success rate of phase unwrapping will be affected by gamma distortion a lot. So, we usually eliminate the gamma distortion by increasing the number of shifts or taking an advanced calibration procedure [26].

5. Conclusion

In this paper, we propose a real-time phase unwrapping method to unwrap phase flexibly and automatically. We derived a mathematical model for wrapped phases and fringe orders by using geometry analysis. Though, with analyzing the model, fringe orders can be determined, we choose an automatically built 1-D or 2-D LUT according to the model to solve the fringe orders. Considering the dominant influence of the defocus effect on phase unwrapping, we derived an error model to find the optimal reference frequencies. Experimental results verify the correctness and efficiency of the proposed method. Although the proposed method using a 2-D LUT is faster than that of a 1-D LUT. The size of the 2-D LUT is much larger than 1-D LUT. Also, the size of 2-D LUT is related to quantization error which we have ignored in this paper because only indices close to the boundary of the stripe in the 2-D LUT may correspond to wrong fringe orders. In future works, we will work on simplifying the 2-D LUT and introducing interpolation to avoid the quantization error as well as perform optimal highest frequency selection.

Funding

National Natural Science Foundation of China (NSFC #61473198); Science and Technology Support Program of Sichuan Province, China (#2018GZ0198); Science and Technology Support Program of Chengdu City, China (#2018-YFYF-00029-GX); Intel Corporation and the National Science Foundation (1539157).

Acknowledgments

Portions of this work were presented at the Emerging Digital Micromirror Device Based Systems and Applications X (SPIE Photonics West OPTO) in 2018, Universal phase unwrapping for phase measuring profilometry using geometry analysis. The contributions of Dr. Daniel L. Lau have been supported by Intel Corporation and the National Science Foundation under contract No. 1539157 and the Visual and Experiential Computing initiative. Dr. Daniel L. Lau is a Professor at the University of Kentucky and a Founder of Seikowave Inc., a private company that designs and sells structured light scanners.

This paper is dedicated to, a friend forever, Dr. Wei WU.

Optics EXPRESS

References

1. R. M. Goldstein, H. A. Zebker, and C. L. Werner, "Satellite radar interferometry: two-dimensional phase unwrapping," Radio Sci. **23**, 713–720 (1988).
2. S. Zhang, X. Li, and S.-T. Yau, "Multilevel quality-guided phase unwrapping algorithm for real-time three-dimensional shape reconstruction," Appl. Opt. **46**, 50–57 (2007).
3. M. Zhao, L. Huang, Q. Zhang, X. Su, A. Asundi, and Q. Kemao, "Quality-guided phase unwrapping technique: comparison of quality maps and guiding strategies," Appl. Opt. **50**, 6214–6224 (2011).
4. H. Zhong, J. Tang, and S. Zhang, "Phase quality map based on local multi-unwrapped results for two-dimensional phase unwrapping," Appl. Opt. **54**, 739–745 (2015).
5. J. M. Huntley and H. Saldner, "Temporal phase-unwrapping algorithm for automated interferogram analysis," Appl. Opt. **32**, 3047–3052 (1993).
6. J. Li, L. G. Hassebrook, and C. Guan, "Optimized two-frequency phase-measuring-profilometry light-sensor temporal-noise sensitivity," J. Opt. Soc. Am. A **20**, 106–115 (2003).
7. C. E. Towers, D. P. Towers, and J. D. Jones, "Time efficient Chinese remainder theorem algorithm for full-field fringe phase analysis in multi-wavelength interferometry," Opt. Express **12**, 1136–1143 (2004).
8. M. Zhang, Q. Chen, T. Tao, S. Feng, Y. Hu, H. Li, and C. Zuo, "Robust and efficient multi-frequency temporal phase unwrapping: optimal fringe frequency and pattern sequence selection," Opt. Express **25**, 20381–20400 (2017).
9. Y. Wang, K. Liu, Q. Hao, D. L. Lau, and L. G. Hassebrook, "Period coded phase shifting strategy for real-time 3-d structured light illumination," IEEE Trans. Image Process. **20**, 3001–3013 (2011).
10. S. Zhang, "Digital multiple wavelength phase shifting algorithm," Proc. SPIE **7432**, 74320N (2009).
11. C. Zuo, L. Huang, M. Zhang, Q. Chen, and A. Asundi, "Temporal phase unwrapping algorithms for fringe projection profilometry: A comparative review," Opt. Lasers Eng. **85**, 84–103 (2016).
12. K. Creath, "Step height measurement using two-wavelength phase-shifting interferometry," Appl. Opt. **26**, 2810–2816 (1987).
13. J. Long, J. Xi, M. Zhu, W. Cheng, R. Cheng, Z. Li, and Y. Shi, "Absolute phase map recovery of two fringe patterns with flexible selection of fringe wavelengths," Appl. Opt. **53**, 1794–1801 (2014).
14. H. Li, Y. Hu, T. Tao, S. Feng, M. Zhang, Y. Zhang, and C. Zuo, "Optimal wavelength selection strategy in temporal phase unwrapping with projection distance minimization," Appl. Opt. **57**, 2352–2360 (2018).
15. Y. An, J.-S. Hyun, and S. Zhang, "Pixel-wise absolute phase unwrapping using geometric constraints of structured light system," Opt. Express **24**, 18445–18459 (2016).
16. C. Zuo, Q. Chen, G. Gu, S. Feng, and F. Feng, "High-speed three-dimensional profilometry for multiple objects with complex shapes," Opt. Express **20**, 19493–19510 (2012).
17. M. Servin, M. Padilla, and G. Garnica, "Super-sensitive two-wavelength fringe projection profilometry with 2-sensitivities temporal unwrapping," Opt. Lasers Eng. **106**, 68–74 (2018).
18. J.-S. Hyun and S. Zhang, "Enhanced two-frequency phase-shifting method," Appl. Opt. **55**, 4395–4401 (2016).
19. V. Gushov and Y. N. Solodkin, "Automatic processing of fringe patterns in integer interferometers," Opt. Lasers Eng. **14**, 311–324 (1991).
20. J. Zhong and M. Wang, "Phase unwrapping by lookup table method: application to phase map with singular points," Opt. Eng. **38**, 2075–2081 (1999).
21. Y. Ding, J. Xi, Y. Yu, and J. F. Chicharo, "Recovering the absolute phase maps of two fringe patterns with selected frequencies," Opt. Lett. **36**, 2518–2520 (2011).
22. Y. Ding, J. Xi, Y. Yu, W. Cheng, S. Wang, and J. F. Chicharo, "Frequency selection in absolute phase maps recovery with two frequency projection fringes," Opt. Express **20**, 13238–13251 (2012).
23. K. Liu, Y. Wang, D. L. Lau, Q. Hao, and L. G. Hassebrook, "Dual-frequency pattern scheme for high-speed 3-D shape measurement," Opt. Express **18**, 5229–5244 (2010).
24. Y. Wang, K. Liu, Q. Hao, X. Wang, D. L. Lau, and L. G. Hassebrook, "Robust active stereo vision using Kullback-Leibler divergence," IEEE Trans. Pattern Anal. Mach. Intell. **34**, 548–563 (2012).
25. C. Zhang, H. Zhao, and L. Zhang, "Fringe order error in multifrequency fringe projection phase unwrapping: reason and correction," Appl. Opt. **54**, 9390–9399 (2015).
26. K. Liu, Y. Wang, D. L. Lau, Q. Hao, and L. G. Hassebrook, "Gamma model and its analysis for phase measuring profilometry," J. Opt. Soc. Am. A **27**, 553–562 (2010).
27. L. Rao and F. Da, "Local blur analysis and phase error correction method for fringe projection profilometry systems," Appl. Opt. **57**, 4267–4276 (2018).
28. X. Zhou and X. Su, "Effect of the modulation transfer function of a digital image-acquisition device on phase-measuring profilometry," Appl. Opt. **33**, 8210–8215 (1994).
29. Z. Li and Y. Li, "Gamma-distorted fringe image modeling and accurate gamma correction for fast phase measuring profilometry," Opt. Lett. **36**, 154–156 (2011).